A Higher-Order Closure Model with an Explicit PBL Top

CARA-LYN LAPPEN, DAVID RANDALL, AND TAKANOBU YAMAGUCHI

Colorado State University, Fort Collins, Colorado

(Manuscript received 26 May 2009, in final form 31 August 2009)

ABSTRACT

In 2001, the authors presented a higher-order mass-flux model called ''assumed distributions with higher-order closure'' (ADHOC 1), which represents the large eddies of the planetary boundary layer (PBL) in terms of an assumed joint distribution of the vertical velocity and scalars. In a subsequent version (ADHOC 2) the authors incorporated vertical momentum fluxes and second moments involving pressure perturbations into the framework. These versions of ADHOC, as well as all other higher-order closure models, are not suitable for use in large-scale models because of the high vertical and temporal resolution that is required. This high resolution is needed mainly because higher-order closure (HOC) models must resolve discontinuities at the PBL top, which can occur anywhere on a model's Eulerian vertical grid. This paper reports the development of ADHOC 3, in which the computational cost of the model is reduced by introducing the PBL depth as an explicit prognostic variable. ADHOC 3 uses a stretched vertical coordinate that is attached to the PBL top. The discontinuous jumps at the PBL top are ''hidden'' in the layer edge that represents the PBL top. This new HOC model can use much coarser vertical resolution and a longer time step and is thus suitable for use in large-scale models. To predict the PBL depth, an entrainment parameterization is needed. In the development of the model, the authors have been led to a new view of the old problem of entrainment parameterization. The relatively detailed information available in the HOC model is used to parameterize the entrainment rate. The present approach thus borrows ideas from mixed-layer modeling to create a new, more economical type of HOC model that is better suited for use as a parameterization in large-scale models.

1. Introduction

Large-eddy simulation (LES) is the most physically complete approach to simulation of the planetary boundary layer (PBL) and cumulus convection, but it is currently much too expensive for use in large-scale models.

Less expensive approaches include mixed-layer models (e.g., Lilly 1968; Ball 1960), in which conservative variables are assumed independent with height inside the PBL, but ''jumps'' or near-discontinuities of these same variables are permitted at the PBL top. The depth of the PBL is introduced as an explicit model variable, usually determined with a prognostic equation involving the rate of turbulent entrainment across the PBL top. Mixed-layer models have been used as PBL parameterizations in large-scale models (e.g., Deardorff 1972; Randall 1976; Suarez et al. 1983; Randall et al. 1985; Medeiros et al. 2005). A problem with mixed-layer models is that the PBL is often not well mixed, especially at night.

Higher-order closure (HOC) has also been proposed for use in parameterization of the PBL in large-scale models (e.g., Mellor and Yamada 1974; Miyakoda and Sirutis 1977). Even the simplest HOC models represent PBL processes in considerably more detail than mixed-layer models. In particular, HOC models are capable of predicting the internal vertical structure of the PBL. They are also capable of representing a shallow cumulus layer. HOC models determine the PBL depth implicitly, as the level above which the turbulence intensity is negligible. In practice, HOC models need vertical grid spacings on the order of 50 m or less, with correspondingly short time steps. The high vertical resolution is needed mainly because HOC models must resolve the important jumps at the PBL top, which can occur anywhere on a model's Eulerian vertical grid. Partly for this reason, HOC models have not been extensively used as parameterizations for large-scale models.

In this paper, we report the development of a new kind of HOC model in which the PBL top is explicitly predicted, as in a mixed-layer model. We also permit discontinuities at the PBL top, as in a mixed-layer model. Instead of the height coordinate that was used in earlier

Corresponding author address: Cara-Lyn Lappen, 87 Sortais Road, Durango, CO 81301.
E-mail: lappen7@gmail.com

DOI: 10.1175/2009JAS3205.1

versions of our model—called ''assumed distributions with higher-order closure'' (ADHOC)—our new approach follows Konor et al. (2009) by using a stretched vertical coordinate that is attached to the PBL top and that provides a fixed number of layers within the PBL, regardless of the depth of the PBL. The discontinuous jumps are ''hidden'' in the layer edge that represents the PBL top. Because the interior structure of the PBL is vertically smooth, our new HOC model can use much coarser vertical resolution inside the PBL, and a longer time step, relative to a conventional HOC model. To predict the PBL depth, an entrainment parameterization is needed, but it can make use of the relatively detailed information available in the HOC model. Our approach thus borrows ideas from mixed-layer modeling to create a new, more economical type of HOC model that is better suited for use as a parameterization in large-scale models.

This practical objective is not the only point of our study, however. In the development of the model, we have been led to a new view of the old problem of entrainment parameterization.

The particular approach that we take to HOC makes use of assumed distributions, which is reflected in the model name (Lappen and Randall 2001a,b,c; hereafter, LRa, LRb, and LRc; the three conjointly are cited as LRabc). The use of assumed distributions can be considered to have originated with the work of Sommeria and Deardorff (1977) and Mellor (1977). They assumed a joint Gaussian distribution for fluctuations of total water mixing ratio q_t and liquid water potential temperature θ_l on a constant height surface. Using this assumed joint distribution, they were able to compute the fractional cloudiness in a turbulent layer, using as input the means, variances, and covariance of q_t and θ_l.

Randall (1987) extended this approach by introducing assumed *three-way* joint distributions of q_t, θ_l, and the vertical velocity w. This generalization permitted diagnosis of the vertical fluxes of q_t and θ_l, as well as the fractional cloudiness. The idea was worked out much more completely, and extensively tested, by LRabc, who described the first version of ADHOC.

ADHOC 1 addressed only scalar transports. In more recent work, we have described ADHOC 2, which incorporates vertical fluxes of horizontal momentum and also second moments involving the pressure (Lappen and Randall 2005, 2006).

This paper reports the development of ADHOC 3, in which, as described above, we reduce the computational cost of the model by introducing the PBL depth as an explicit, prognostic variable. Jumps are allowed at the PBL top. The internal vertical structure of the PBL is resolved, although it is our intention to do this with just a few discrete layers. We use a stretched vertical coordinate that is attached to the PBL top, as in the model of Suarez et al. (1983). Konor et al. (2009) have recently demonstrated the potential of such a multilevel bulk approach, although they used very simple parameterizations of the turbulent fluxes and the entrainment rate. ADHOC 3 is suitable for use as a PBL parameterization in the model of Konor et al. (2009).

Section 2 of this paper gives a description of ADHOC 3, including the stretched vertical coordinate and the boundary conditions at the PBL top. The vertically discrete version is explained in the appendix. Section 3 presents our entrainment parameterization, including the results of tests against various standard cases. Section 4 discusses the sensitivity of the model to vertical resolution within the PBL. Section 5 gives a summary and conclusions.

2. ADHOC 3

a. Basics

ADHOC was developed in the late 1990s by combining higher-order closure and mass-flux closure (MFC) into a unified framework (LRabc; Randall et al. 1992). At that time (and still to a large extent), large-scale models use separate schemes for the PBL and for shallow and deep convection. ADHOC attempts to bridge the gaps separating these schemes and provide a single set of equations that will be useful for the parameterization of *both* the PBL and shallow cumulus convection, in a unified framework.

ADHOC makes use of an assumed joint probability distribution for the variables of interest, and the equations typically used in HOC models can be derived by integrating over the distribution. The prognostic variables of ADHOC are the mean state, the second and third moments of the vertical velocity, and all the vertical fluxes. All of the parameters of the distribution can be determined from the predicted moments; thereafter, the joint distribution is effectively known, and so any and all moments can be constructed as needed. In this way, the usual closure problem of ''higher moments'' is avoided.

In principle, ADHOC can use any simple probability distribution function (PDF) as its base distribution. We chose to use a top-hat PDF for simplicity. To diagnose the parameters of this PDF as applied to the vertical velocity, it suffices to know the first three moments of the vertical velocity (i.e., $\overline{w}$, $\overline{w'w'}$, and $\overline{w'w'w'}$; see LRa). Randall et al. (1992) showed that the updraft area fraction (uaf) and the convective mass flux (M_c) can be diagnosed if these three moments of the vertical velocity are known. These relationships are

$$\text{uaf} = \frac{1}{2} - \frac{S_w}{2\sqrt{4 + S_w^2}} \tag{2.1}$$

and

$$M_c = \frac{\rho\sqrt{\overline{w'w'}}}{\sqrt{4 + S_w^2}}, \tag{2.2}$$

where $S_w = \overline{w'w'w'}/(\overline{w'w'})^{3/2}$ is the vertical velocity skewness.

In ADHOC, we predict $\overline{w'w'}$ and $\overline{w'w'w'}$. We can then diagnose uaf and M_c using Eqs. (2.1) and (2.2). The prognostic equations that we use for $\overline{w'w'}$ and $\overline{w'w'w'}$ are the usual HOC equations for these moments, as applied specifically to the top-hat PDF (see LRa; de Roode et al. 2000). We can write the top-hat formulas for these moments as

$$\overline{w'w'} = \text{uaf}(1 - \text{uaf})(w_{\text{up}} - w_{\text{dn}})^2 \tag{2.3}$$

and

$$\overline{w'w'w'} = \text{uaf}(1 - \text{uaf})(1 - 2\text{uaf})(w_{\text{up}} - w_{\text{dn}})^3, \tag{2.4}$$

where $w_{\text{up}}(w_{\text{dn}})$ is the vertical velocity in the updraft (downdraft). In addition, we can write the vertical flux of a quantity (ψ) as

$$\overline{w'\psi'} = \text{uaf}(1 - \text{uaf})(w_{\text{up}} - w_{\text{dn}})(\psi_{\text{up}} - \psi_{\text{dn}}). \tag{2.5}$$

In ADHOC, we predict these vertical fluxes, as well as the mean value of ψ. This enables us to diagnose the updraft and downdraft values of ψ, as well as all moments involving ψ and/or the vertical velocity.

A HOC equation can be used to predict each of the moments on the left-hand side of Eqs. (2.3)–(2.5) and a mass-flux equation predicting each of the quantities on the right-hand side of Eqs. (2.3)–(2.5). If we require that these two sets of equations to be consistent with each other, we obtain a single system of equations that combines mass flux and HOC.

An issue with this approach is that the mass-flux formulas given by Eqs. (2.3)–(2.5) do not give 100% of the true variance and/or covariance (Businger and Oncley 1990; Young 1988; Wyngaard and Moeng 1992; Wang and Stevens 2000; de Laat and Duynkerke 1998) because the mass-flux quantities only represent the large eddies, while the ensemble-averaged moments are supposed to represent all scales of motion. As recommended by Petersen et al. (1999), we use a subplume-scale model in ADHOC to represent the smaller scales of motion not represented by the mass-flux formulas. Thus, we force consistency between the HOC and mass-flux moments by summing the subplume scale and the mass-flux scale contributions to the higher moments (see LRb).

b. Stretched vertical coordinate

The often observed sharp jumps at the PBL top can be directly resolved only through the use of very high vertical resolution. In large-scale models, such high resolution is unacceptably expensive. One way around this problem is to use a vertical coordinate in which the PBL top is a coordinate surface (Suarez et al. 1983; Randall et al. 1985; Konor and Arakawa 1997; Medeiros et al. 2005; Konor et al. 2009; Kasahara 1974). In such a model, the inversion height is known and thus not as much resolution is needed.

Following Suarez et al. (1983), our σ coordinate is defined by

$$\sigma \equiv 1 + \frac{p - p_B}{\pi} \text{ in the PBL} \tag{2.6}$$

and

$$\sigma \equiv \frac{p - p_T}{p_B - p_T} \text{ above the PBL}, \tag{2.7}$$

where p is the pressure; $\pi = p_S - p_B$ is the pressure thickness of the PBL; and the subscripts T, B, and S refer to the top of the atmosphere, the top of the PBL, and the surface, respectively. Using these definitions, $\sigma = 2$ at the surface, $\sigma = 1$ at the PBL top, and $\sigma = 0$ at the top of the atmosphere. The ''jump layer'' at the PBL top is bounded below by level B and above by level B+. (See Fig. A1.) Discontinuities are hidden in the layer edge at the PBL top. Discontinuous fields include both the mean state (e.g., the mean temperature changes discontinuously upward) and higher moments (e.g., the turbulent fluxes that affect mean-state variables decrease upward discontinuously to zero across the PBL top). Above level B+, all turbulent fluctuations are assumed to vanish.

We start with the flux-form conservation equation for an arbitrary scalar, A:

$$\frac{\partial(\pi A)}{\partial t} + \nabla_\sigma \cdot (\pi \mathbf{v} A) + \frac{\partial(\pi\dot{\sigma}A)}{\partial\sigma} = g\frac{\partial F_A}{\partial\sigma} + \pi S_A. \tag{2.8}$$

Here F_A is the turbulent flux of A, and S_A represents any sources or sinks of A, per unit mass. We have neglected, for simplicity, the effects of deep cumulus clouds. For $A \equiv 1$, (2.8) reduces to the continuity equation:

$$\frac{\partial \pi}{\partial t} + \nabla \cdot (\pi \mathbf{v}) + \frac{\partial (\pi \dot{\sigma})}{\partial \sigma} = 0. \tag{2.9}$$

If we integrate Eq. (2.9) over all PBL layers and use the boundary condition that no mass crosses the earth's surface—that is, $(\pi\dot{\sigma})_S = 0$—we obtain

$$\frac{\partial \pi}{\partial t} + \nabla \cdot \left(\int_S^B \pi \mathbf{v}\, d\sigma \right) = (\pi \dot{\sigma})_B. \tag{2.10}$$

The mass flux across the PBL top, $(\pi\dot{\sigma})_B$, consists of downward turbulent entrainment, so that

$$(\pi \dot{\sigma})_B = gE. \tag{2.11}$$

Suppose that $(\pi\dot{\sigma})_B$ has been determined by using an entrainment parameterization on the right-hand side of (2.11). Then (2.10) determines $\partial\pi/\partial t$; that is, we can predict the pressure thickness of the PBL. In addition, $\partial\pi/\partial t$ from (2.10) can be substituted back into (2.9) to obtain $\pi\dot{\sigma}$ as a function of height throughout the depth of the PBL. We can then "vertically advect" an arbitrary quantity within the PBL, as required in (2.8). This is the approach used by Konor et al. (2009). For more details, see the appendix.

To express conservation of A within the infinitesimal layer at the PBL top, following Lilly (1968), we integrate (2.8) across the PBL top, and use Liebnitz's rule, to obtain

$$-\Delta(\pi \dot{\sigma} A) = g(F_A)_B + \pi \int_{\sigma_{B+}}^{\sigma_B} S_A\, d\sigma, \tag{2.12}$$

where $\Delta(\cdot) \equiv (\cdot)_{z_B+\varepsilon} - (\cdot)_{z_B-\varepsilon}$ is the jump in A. Here we have used our assumption that F_A vanishes above the PBL top. For the special case $A \equiv 1$, (2.12) reduces to

$$\Delta(\pi \dot{\sigma}) = 0. \tag{2.13}$$

Using (2.11) and (2.13), and hydrostatics, we can rewrite (2.12) as

$$-E\Delta A = (F_A)_B + \int_{z_B-\varepsilon}^{z_B+\varepsilon} \rho S_A\, dz. \tag{2.14}$$

This equation can be used to determine $(F_A)_B$ if the entrainment rate and $\int_{z_B-\varepsilon}^{z_B+\varepsilon} \rho S_A\, dz$ are known. It is important to note that because the range of integration is very small, the source term on the right-hand side (2.14) is negligible unless S_A is very large at the PBL top, as in the case of concentrated radiative cooling at a cloud top (Lilly 1968).

3. Entrainment parameterization

Entrainment has been one of the more challenging issues in PBL modeling over the last 40 years. Dozens of papers describe parameterizations for entrainment in cloud-topped, smoke-filled, and clear convective boundary layers (see the review by Stevens 2002). In general, when the turbulence is stronger, the entrainment rate is more rapid. Entrainment is usually a self-limiting process, however, because it brings warmer, drier air down into the PBL. This produces a negative buoyancy flux, weakening the turbulence that drives the entrainment.

In this section, we present a new entrainment parameterization derived by applying the HOC equations at the PBL top. We test the model using data from the Wangara experiment (Clark et al. 1971; André et al. 1978), a smoke cloud case (Bretherton et al. 1999), an idealized case with cloud-top entrainment instability (CTEI; Yamaguchi and Randall 2008, hereafter YR08), a marine stratocumulus (MSc) case [the Second Dynamics and Chemistry of Marine Stratocumulus field study (DYCOMS II) case RF01; Stevens et al. 2003], and LES results from the System for Atmospheric Modeling (SAM; Khairoutdinov and Randall 2003).

We parameterize the entrainment rate by considering the budget of $\overline{w'w'}$ and $\overline{w'w'w'}$ in the vicinity of the PBL top. As discussed below, it emerges that the key term in the equation for $\overline{w'w'}$ is the divergence of the flux due to $\overline{w'w'w'}$. When $\overline{w'w'w'}$ is positive (upward) at the PBL top, as in clear convective and shallow cumulus layers, narrow, intense updrafts impinge on the inversion base, supplying energy that can be used for entrainment. When $\overline{w'w'w'}$ is negative at the PBL top, as in stratocumulus layers, narrow, intense downdrafts drain energy away from the inversion base, inhibiting entrainment.

The previous versions of ADHOC have predicted the second and third moments of the vertical velocity ($\overline{w'w'}$ and $\overline{w'w'w'}$). ADHOC 3 is no exception. We predict these moments using Eq. (2.8) with $A \equiv \overline{w'w'}$ ($F_A \equiv \rho\overline{w'w'w'}$) and $A = \overline{w'w'w'}$ ($F_A = \rho\overline{w'w'w'w'}$), respectively. For the PBL top jump layer, we use Eq. (2.14) to write

$$E\overline{w'w'_B} = \rho\overline{w'w'w'_B} + \int_{z_B-\varepsilon}^{z_B+\varepsilon} \rho S_{\overline{w'w'}}\, dz \tag{3.1}$$

and

$$E\overline{w'w'w'_B} = \rho\overline{w'w'w'w'_B} + \int_{z_B-\varepsilon}^{z_B+\varepsilon} \rho S_{\overline{w'w'w'}}\, dz. \tag{3.2}$$

Here we have used our assumption that all turbulent fluctuations vanish above the PBL top. In Eqs. (3.1) and (3.2),

$$\rho S_{\overline{w'w'}} \equiv \frac{2g}{C_p T_0}\rho\overline{w's'_v} + P_{\overline{w'w'}} - M_c\left(\frac{C_E}{L_{\rm dn}} + \frac{C_D}{L_{\rm up}}\right)\overline{w'w'} \tag{3.3}$$

and

$$\rho S_{\overline{w'w'w'}} = \frac{2g}{C_p T_0}\rho\overline{w's'_v}\left(\frac{\overline{w'w'w'}}{\overline{w'w'}}\right) + P_{\overline{w'w'w'}} - M_c\left(\frac{C_E}{L_{\rm dn}} + \frac{C_D}{L_{\rm up}}\right)\overline{w'w'w'}, \tag{3.4}$$

where C_p is the specific heat of air at constant pressure, T_0 is a reference temperature, $L_{\rm dn}(L_{\rm up})$ is the downward (upward) turbulent length scale, $P_{\overline{w'w'_B}}$ and $P_{\overline{w'w'w'_B}}$ are the pressure terms, and M_c is the convective mass flux defined by Eq. (2.2). The last term on the right-hand side of Eqs. (3.3) and (3.4) represents the effects of dissipation, in which C_E and C_D are constants defined in LRb. In Eq. (3.4), we have also used the ADHOC relation

$$\overline{w'w's'_v} = \overline{w's'_v}\left(\frac{\overline{w'w'w'}}{\overline{w'w'}}\right). \tag{3.5}$$

We now rewrite Eqs. (3.1) and (3.2) respectively as

$$\overline{w'w'_B}E = \rho\overline{w'w'w'_B} + \int_{z_B-\varepsilon}^{z_B+\varepsilon}\frac{2g}{C_p T_0}\rho\overline{w's'_v}\,dz \tag{3.6}$$

and

$$\overline{w'w'w'_B}E = \rho\overline{w'w'w'w'_B} + \int_{z_B-\varepsilon}^{z_B+\varepsilon}\frac{g}{C_p T_0}\rho\overline{w's'_v}\left(\frac{\overline{w'w'w'}}{\overline{w'w'}}\right)dz. \tag{3.7}$$

In Eqs. (3.6) and (3.7), we have neglected the effects of dissipation and the pressure terms in the inversion jump layer. The LES results shown in Fig. 1 justify this simplifying assumption. In the yellow shaded area of this figure, the two dominant terms are the transport and the buoyancy. Directly below the thin inversion layer, pressure assumes a more important role. The dissipation has a small role in the budget, but only below the inversion layer.

The virtual dry static energy flux at the inversion base, $\overline{w's'_{vB}}$, is determined by the entrainment rate and the strength of possible radiative cooling concentrated at the top of the PBL (e.g., Lilly 1968). The entrainment term takes different forms depending on whether or not the upper portion of the PBL contains cloud. In general, we can write

$$\rho\overline{w's'_{vB}} = -E\Delta\tau + C_R\Delta R, \tag{3.8}$$

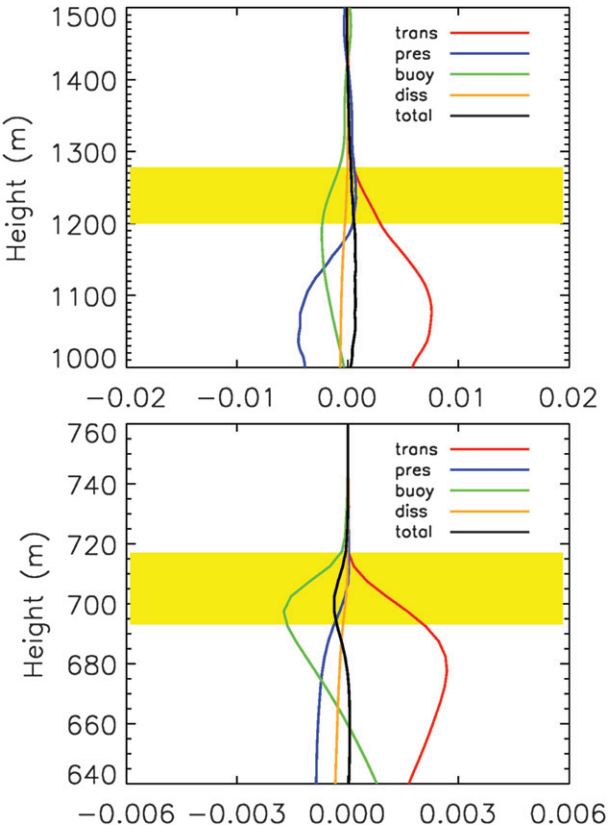

FIG. 1. LES budgets of $\overline{w'w'}$ in the inversion from (top) Wangara and (bottom) the smoke cloud. The yellow shading indicates the inversion area. All curves have been diagnosed from SAM's simulation of Wangara and the smoke cloud case described by Bretherton et al. (1999).

where ΔR is the radiative flux jump across the PBL top when cloud (or smoke cloud) is present, and the form of $\Delta\tau$ varies depending on the presence or absence of cloud (or smoke cloud), as first pointed out by Lilly (1968). Note that C_R is equal to either 1 or 0 depending on whether or not a cloud is present.

Using Eq. (3.8), we can rewrite Eq. (3.6) as

$$\overline{w'w'_B}E = \rho\overline{w'w'w'_B} + \frac{2g\delta z}{C_p T}(-E\Delta\tau + C_R\Delta R), \tag{3.9}$$

where δz is a depth scale (discussed below). Solving for $\overline{w'w'w'_B}$, we get

$$\rho\overline{w'w'w'_B} = E(\overline{w'w'_B} + B) - \frac{2g}{C_p T_0}\delta z C_R\Delta R, \tag{3.10}$$

where $B \equiv (2g\delta z/C_p T)\Delta\tau$ is the buoyancy term at level B (PBL top).

Similarly, substituting Eq. (3.8) into Eq. (3.7) and solving for $\overline{w'w'w'_B}$, we get

$$\overline{w'w'w'_B} = \frac{\rho(\overline{w'w'_B})(\overline{w'w'w'w'_B})}{E(\overline{w'w'_B} + B) - \dfrac{2g}{C_p T_0}\delta z C_R \Delta R}. \quad (3.11)$$

If we now set Eq. (3.10) equal to Eq. (3.11), we have two unknowns (E and $\overline{w'w'w'w'_B}$). In order to alleviate one unknown, we use the quasi-normal approximation (Millionshchikov 1941; André et al. 1978)

$$\overline{w'w'w'w'} = 3(\overline{w'w'})^2 \quad (3.12)$$

in Eq. (3.11). This yields

$$\overline{w'w'w'_B} = \frac{3\rho(\overline{w'w'})^3}{E(\overline{w'w'_B} + B) - \dfrac{2g\delta z}{C_p T_0} C_R \Delta R}. \quad (3.13)$$

We test the quasi-normal approximation by calculating horizontal averages of the second and fourth moments of w' using data from SAM's simulation of Wangara and the Global Energy and Water Cycle Experiment (GEWEX) Cloud System Study (GCSS) smoke cloud cases. These results were calculated at 2 p.m. for Wangara and at hour 3 for the smoke cloud simulation. The results of this, which are shown in Fig. 2, support using the quasi-normal approximation in the inversion jump layer for these cases.

We now compare Eq. (3.13) with Eq. (3.10), which leads to

$$\left[(\overline{w'w'_B} + B)E - \frac{2g\delta z}{C_p T_0} C_R \Delta R\right]^2 = 3(\overline{w'w'_B})^3, \quad (3.14)$$

which can be solved in a quadratic equation for E:

$$E = \frac{\pm\sqrt{3}(\overline{w'w'_B})^{3/2} + \dfrac{2g\delta z}{C_p T_0} C_R \Delta R}{\overline{w'w'_B} + B}. \quad (3.15)$$

This formula is applicable to any PBL. As expected, radiative cooling acts to increase the entrainment rate, while $B > 0$ decreases it.

Equation (3.15) has two roots. For a clear, convective PBL, the second term in the numerator is equal to zero, while the denominator is positive. Thus, we must choose the positive root in order to ensure a positive entrainment rate. In the case of a smoke-filled PBL, the second term in the numerator and the denominator are both positive. Thus, we could choose the negative root and still get positive entrainment. We will discuss this further in section 4b. Finally, for the case of stratocumulus-topped PBLs that exhibit CTEI, the denominator can be negative (see section 4c). Thus, if the first term in the numerator is larger than the second, the negative root must be chosen. In practice, we find that we must choose the negative root for any stratocumulus layer with CTEI (see section 4).

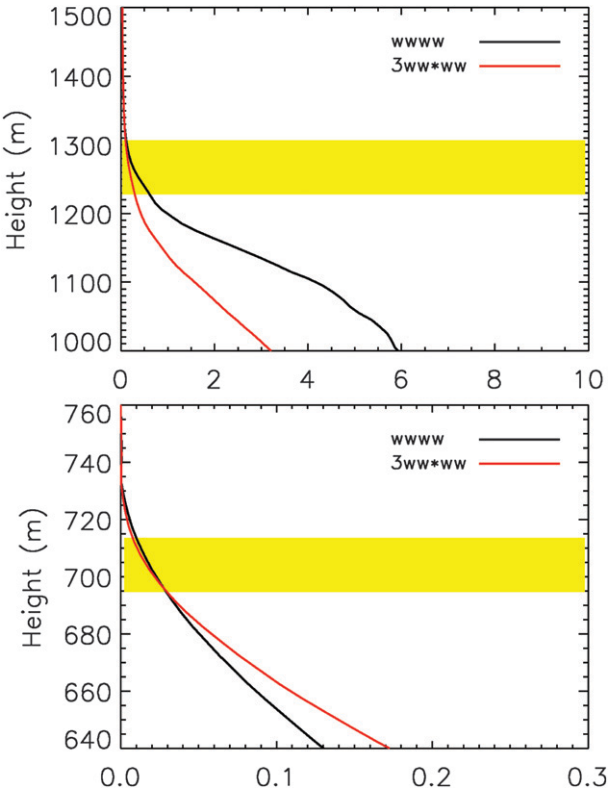

FIG. 2. Quasi-normal approximation as applied to the inversions of (top) Wangara and (bottom) a smoke cloud. The yellow area is the inversion layer. Both the red and black curves have been diagnosed from SAM's simulation of Wangara and the smoke cloud case described by Bretherton et al. (1999).

If we substitute Eq. (3.15) into Eq. (3.10), we get an expression for $\overline{w'w'w'_B}$:

$$\overline{w'w'w'_B} = \pm\sqrt{3}(\overline{w'w'_B})^{3/2}. \quad (3.16)$$

The sign of $\overline{w'w'w'_B}$ depends on the choice of solution in Eq. (3.15). Further discussion of the sign is given in section 4. Figure 3 shows that LES results support the use of Eq. (3.16) for the cases we tested (Wangara, smoke cloud, and DYCOMS).

4. Test cases

a. Clear convective PBL

In a clear, convective boundary layer, $\Delta R = 0$ and $B = (2g\delta z/C_p T)\Delta s_v$ in Eq. (3.15). Thus, the expression for the entrainment rate is

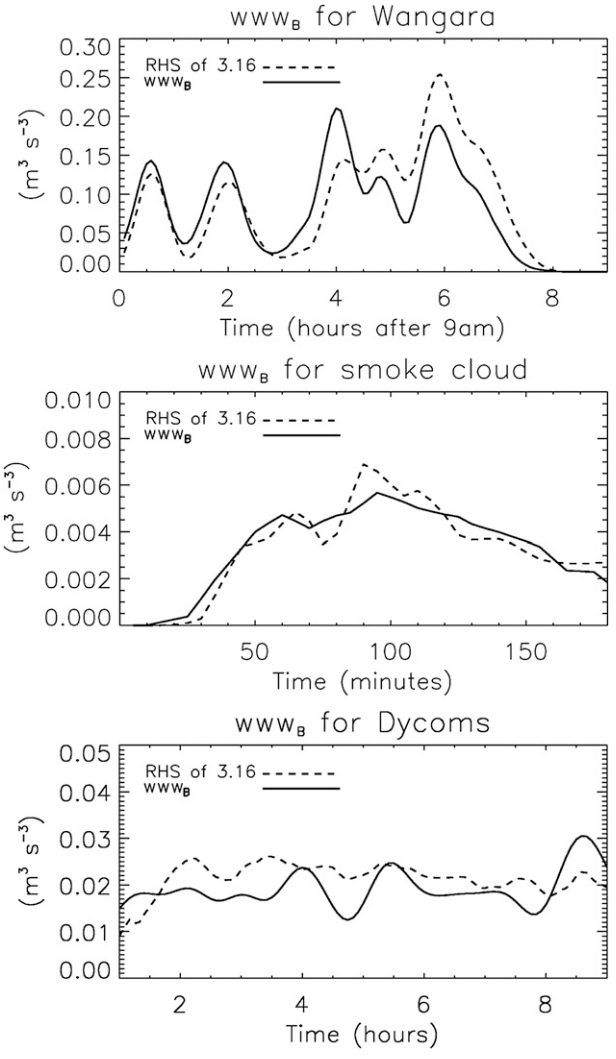

FIG. 3. Comparison of the right and left sides of Eq. (3.16) for (top) Wangara, (middle) smoke cloud, and (bottom) DYCOMS.

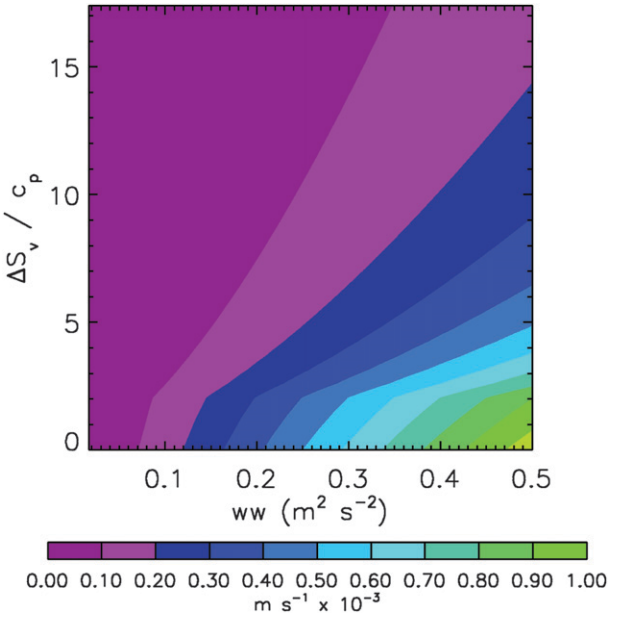

FIG. 4. Entrainment rate vs Δs_v and $\overline{w'w'}$ for the clear convective case.

$$E = \frac{\sqrt{3}\rho(\overline{w'w'_B})^{3/2}}{\overline{w'w'_B} + B}. \tag{4.1}$$

Here we have chosen the positive root for the reasons explained previously. Equation (4.1) says that the entrainment rate increases with stronger turbulence at the PBL top (as measured by $\overline{w'w'_B}$) and decreases as the virtual static energy jump (B) strengthens. This is shown in Fig. 4.

We can compare our expression for entrainment in a clear convective boundary layer to the one that is used in the Colorado State University (CSU) GCM (also see Breidenthal and Baker 1985, hereafter BB85; Siems et al. 1990):

$$E = \frac{b_1\rho\sqrt{e_m}}{1 + b_2 R_{i\Delta}}, \tag{4.2}$$

where

$$R_{i\Delta} = \frac{g\delta z_m \max(\Delta s_v, 0)}{C_p \overline{T}_B e_m}; \tag{4.3}$$

e_m is the integrated turbulence kinetic energy; $b_1 = 0.5$; $b_2 = 0.25$; and δz_m is the mixed layer depth. If we divide the numerator and denominator in Eq. (4.1) by $\overline{w'w'_B}$, we get

$$E = \frac{\sqrt{3}\rho\sqrt{\overline{w'w'_B}}}{1 + \dfrac{B}{\overline{w'w'_B}}}. \tag{4.4}$$

For $\Delta s_v > 0$, Eqs. (4.2) and (4.4) agree when

$$\delta z = \frac{\dfrac{1}{b_1}\sqrt{\dfrac{3\overline{w'w'_B}}{e_m}}\left[1 + \left(\dfrac{g}{C_p T_0}\right)\dfrac{b_2\delta z_m(\Delta s_v)}{e_m}\right] - 1}{\left(\dfrac{g}{C_p T_0}\right)\dfrac{\Delta s_v}{\overline{w'w'_B}}}. \tag{4.5}$$

Since $(g/C_pT_0)b_2\delta z_m(\Delta S_v)/e_m \gg 1$, we can simplify Eq. (4.5) to

$$\delta z; \sqrt{3}\frac{b_1}{b_2}\left(\frac{\overline{w'w'_B}}{e_m}\right)^{3/2}\delta z_m. \qquad (4.6)$$

For all cases in ADHOC 3, we calculate the inversion thickness using Eq. (4.6). As an example, if the vertical velocity variance at the PBL top is ¼ of the vertically averaged TKE and the mixed layer depth is 1000 m, the inversion layer thickness would be approximately 108 m.

WANGARA TEST

To test our parameterization of entrainment for the dry convective PBL, we simulated day 33 of the Wangara experiments (Clark et al. 1971) with ADHOC 3. This is a classic dry convective PBL driven solely by heating of the surface. The mean state and higher-moment profiles in this PBL genre are well understood by the atmospheric science community (e.g., André et al. 1978; Willis and Deardorff 1974; Moeng 1984). We ran the case from 9 a.m. to 6 p.m. using 10 vertical levels in the PBL, and we compare our results to those simulated by SAM.

In SAM, the simulation is conducted for the same 9 h. The domain size is 3.2 km horizontally and 3.0 km vertically. The grid size is 10 m in both the horizontal and vertical directions. The run is forced with observed surface heat and moisture fluxes. The surface momentum fluxes are computed with Monin–Obukhov similarity. Horizontal mean profile data is output as 5-min averages of profiles collected every 20 s.

In Fig. 5, we show a comparison between ADHOC 3 and SAM for the moist static energy $\overline{h}$ and the moist static energy flux $\overline{w'h'}$ at 2 p.m. (6 h into the Wangara simulation). The agreement shows that ADHOC is able to keep the boundary layer well mixed and produce a linearly decreasing flux profile. The boundary layer top height, whose rate of growth is strongly influenced by the entrainment rate, is also in agreement with SAM. We also show $\overline{w'w'w'}$ in this figure. The biggest difference is near the surface where the vertical transport of $\overline{w'w'}$ is negative in ADHOC 3.

We compare the Wangara entrainment rate from ADHOC 3 [using Eq. (4.4)] with that of SAM (Fig. 6). We calculated the SAM entrainment rate using two methods: the method suggested by GCSS and that of YR08. While the GCSS method gives results that are a little noisy, there is some agreement between SAM and ADHOC 3. In this particular case, the ADHOC formula facilitates PBL growth to the proper height.

To directly compare the ADHOC 3 entrainment parameterization for the clear convective boundary layer to other schemes, we have also run ADHOC 3 with the entrainment parameterization of BB85. Figure 7 shows the evolution of $\overline{w'w'}$ in both of these runs, as well as in SAM. We see that the BB85 formulation does increase the PBL top height in time. It does not, however, do it as quickly as the LES, nor does it show the initial speeding up of the PBL top growth between 10 and 11 a.m.

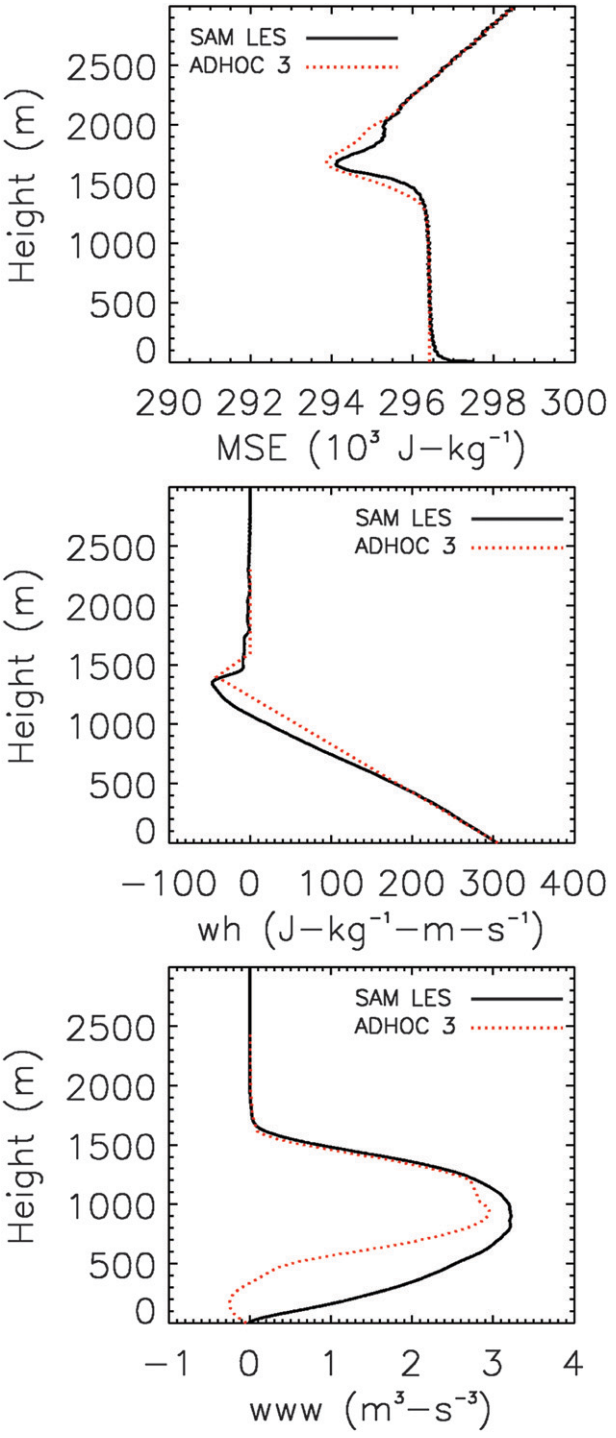

FIG. 5. Comparison of ADHOC 3 and SAM for Wangara run: (top) moist static energy, (middle) moist static energy flux, and (bottom) www. Time shown is 2 p.m.

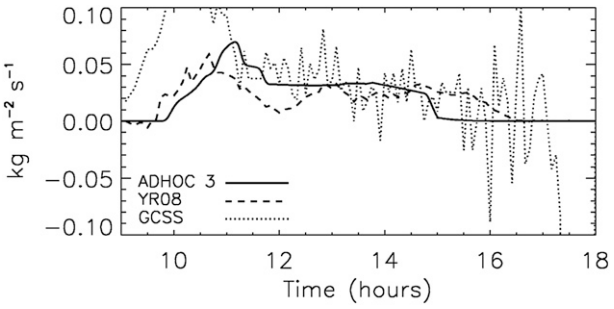

FIG. 6. Comparison of ADHOC 3, SAM, and GCSS entrainment rates for Wangara.

ADHOC 3 agrees with SAM for the PBL top growth rate and shows the rapid evolution of the PBL top between 10 and 11 a.m. It does not, however, produce the same strength turbulence ($\overline{w'w'}$ is about 30% weaker).

Despite the weaker turbulence in ADHOC 3, the PBL top height agrees with that of SAM. This indicates that the ADHOC entrainment formula is more sensitive to the turbulence than that of YR08. This biggest difference between the two formulations is that the ADHOC 3 formula depends on $\overline{w'w'}$ at the PBL top, while the YR08 formula depends on the PBL top flux jumps. The strength of $\overline{w'w'}$ in the ADHOC 3–BB85 run is similar to that of the ADHOC 3–Eq. (4.4) run; however, the PBL top in the former does not rise as high. This is a direct result of the former being a function of the integrated PBL turbulence, while the latter depends only on the turbulence at the PBL top. The dependence on PBL top turbulence clearly has a more pronounced effect on the PBL top growth.

In Fig. 8, we look at the PBL top turbulence by examining $\overline{w'w'w'_B}$. The top panel compares the evolution in time; the bottom panel shows a scatterplot of $\overline{w'w'w'_B}$. The values of $\overline{w'w'w'_B}$ in ADHOC 3 and SAM are highly correlated. In the scatterplot, the points cluster around the diagonal black line (which shows a perfect 1:1 correspondence).

b. *Smoke cloud PBL*

It was postulated in the 1970s (Deardorff 1976; Kahn and Businger 1979; Stage and Businger 1981a,b; Randall 1980; Lilly and Schubert 1980) that the radiative flux divergence in PBL clouds can promote entrainment in two ways. First, if it occurs in the cloud layer itself, it can *indirectly* increase the entrainment by promoting a larger buoyancy flux, leading to more turbulence. Second, if it occurs within the jump layer just above the PBL top, it *directly* affects entrainment by reducing the overall strength of the inversion. After a heated debate in the 1970s about the distribution of radiative cooling in

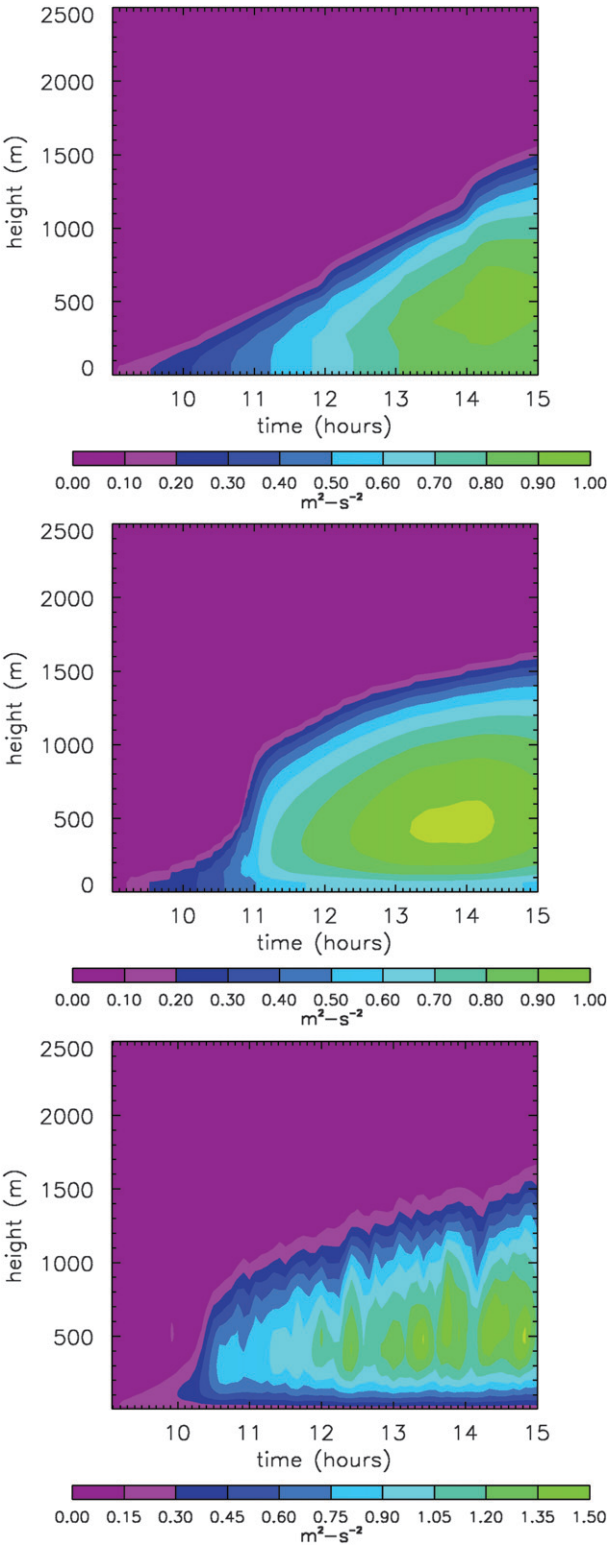

FIG. 7. Comparison of $\overline{w'w'}$ for Wangara: (middle) ADHOC 3 with Eq. (4.4); (top) ADHOC 3 with BB85 [Eq. (4.2)]; (bottom) SAM.

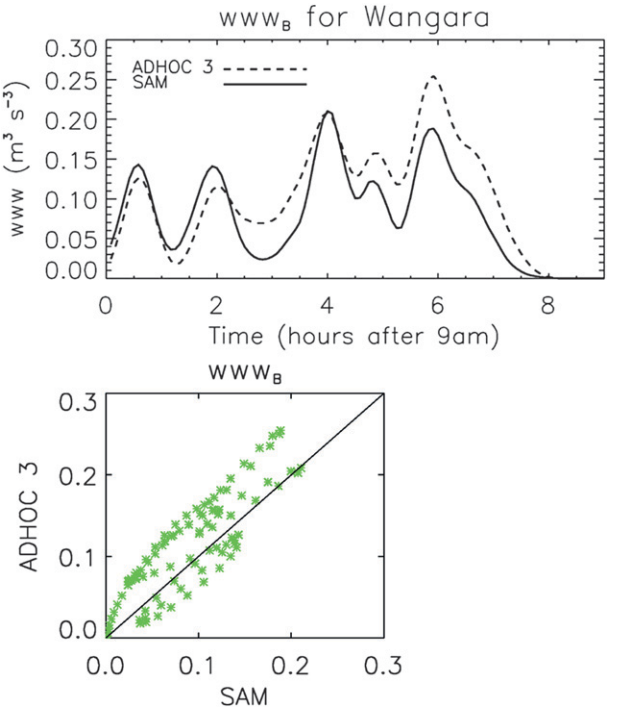

FIG. 8. (top) Comparison of $\overline{w'w'w'}$ at level B for Wangara as calculated by Eq. (3.16). (bottom) Scatterplot for www at level B comparing ADHOC 3 to LES for various times during the simulation. A perfect correlation is given by the diagonal black line.

cloud-topped PBLs, Moeng et al. (1999) showed that almost all of it actually occurs within the cloud layer. Following Moeng's work, we will also assume that this is true.

A radiatively driven *smoke*-cloud PBL is a layer that radiates as liquid water but does not undergo phase changes. The use of smoke cloud as a prototype stratocumulus was suggested by Lilly (1968) and has been used by many investigators (e.g., Schubert et al. 1979; Nieuwstadt and Businger 1984; Moeng et al. 1992; Bretherton et al. 1999). Like stratocumulus, a smoke cloud also emits longwave radiation as a gray body. This results in a sharp divergence of the longwave radiative flux emitted near cloud top and leads to strong radiative cooling, which can buoyantly drive turbulence. Thus, a smoke-topped PBL shares with the stratocumulus-topped PBL the essential features of turbulence and entrainment driven by radiative cooling.

For the smoke-cloud PBL, $C_R = 1$ and $B = (2g\delta z/C_pT)\Delta s_v$ in Eq. (3.15). This makes our entrainment parameterization

$$E = \frac{\pm\sqrt{3}(\overline{w'w'_B})^{3/2} + \dfrac{2g\delta z}{C_p T_0}\Delta R}{\overline{w'w'_B} + B}. \qquad (4.7)$$

Below, we will test both roots of Eq. (4.7) because it is possible to obtain positive entrainment with the negative root.

SMOKE CLOUD TEST

We test our parameterization [Eq. (4.7)] by comparing ADHOC 3 and SAM simulations of the GCSS smoke cloud case from 1995 (Bretherton et al. 1999). In this case, we set the water mixing ratios to zero and start with a prescribed two-layer potential temperature distribution. We introduce a passive smoke tracer s initially equal to 1 in the lower layer and 0 in the upper layer. We then let s be radiatively active by assuming a radiative flux profile in the smoke layer. The flux at the top of the 700-m-thick smoke layer is 60 W m^{-2} and the temperature jump at the inversion is 7 K. This gives a good radiative analog of a stratocumulus cloud with similar radiative flux divergence. The model is run for 3 h and has 10 PBL layers. (For a complete case description, see www.convection.info/blclouds.)

The SAM simulation of this case is also run for 3 h. The horizontal and vertical domains are 3.2 and 1.25 km, respectively. The horizontal grid size is 10 km, while the vertical grid size is 5 m. The time step is 1 s. Horizontal mean profile data is output as 5-min averages of profiles collected every 20 s.

In Fig. 9, we show the simulated profiles (at hour 3) of the smoke concentration s, the smoke flux $\overline{w's'}$, and the moist static energy flux $\overline{w'h'}$, as well as $\overline{w'w'}$ and $\overline{w'w'w'}$. Once again, we see that ADHOC 3 is able to simulate the correct PBL top height with less intense turbulence. This sensitivity is seen in both of our test cases. The poorest agreement is found for $\overline{w'w'w'}$ (which is a measure of the transport of $\overline{w'w'}$). SAM shows more downward transport of $\overline{w'w'}$ (negative $\overline{w'w'w'}$) than ADHOC 3. This is reflected in the lower maximum of $\overline{w'w'}$ for SAM. Overall, however, the mean state and fluxes and the PBL top height agree reasonably well.

Since the PBL top heights are similar after 3 h, we would expect the simulated entrainment rates to agree well between SAM and ADHOC 3. This is plotted in Fig. 10 using the YR08 method in SAM and Eq. (4.7) for ADHOC 3. We have plotted both the positive and negative roots of Eq. (4.7). The methods of YR08 and ADHOC 3 show similar entrainment rates after the first hour of the simulation. YR08 spins up quickly, while ADHOC 3's spinup is more gradual. After an initial 1-h adjustment, they both settle down to approximately the same entrainment value (between 0.0035 and 0.004 kg m^{-2} s^{-1}). The negative root of Eq. (4.7) is clearly not correct for the smoke cloud case. This means that the turbulence term [the $\overline{w'w'_B}$ term in Eq. (4.7)] dominates the radiative cooling term.

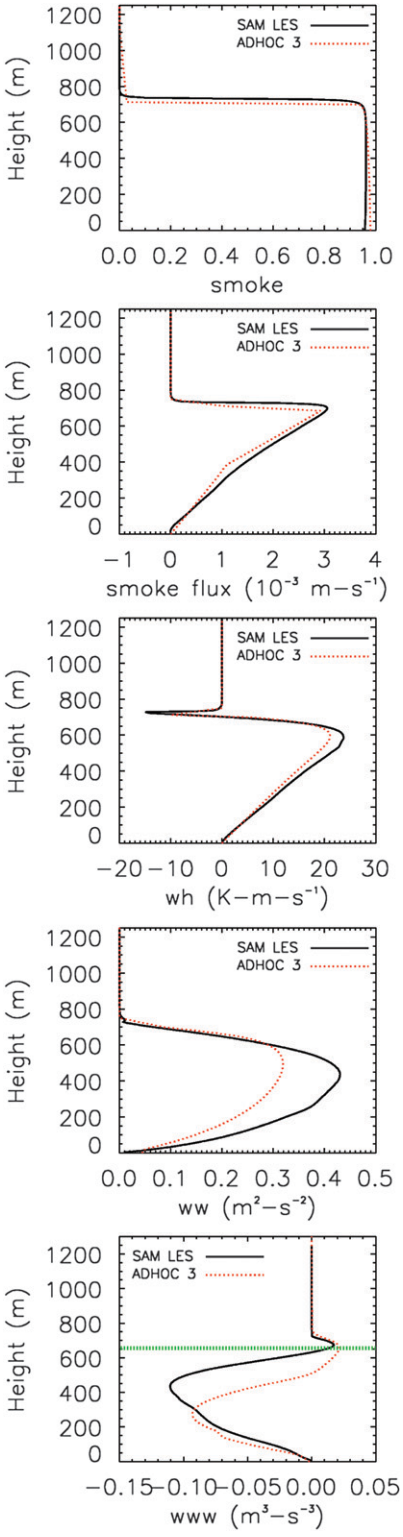

FIG. 9. Comparison of ADHOC 3 and SAM for the GCSS smoke cloud case. From top to bottom: smoke concentration, smoke flux, moist static energy flux, $\overline{w'w'}$, and $\overline{w'w'w'}$. The dotted green line shows the level of the inversion base.

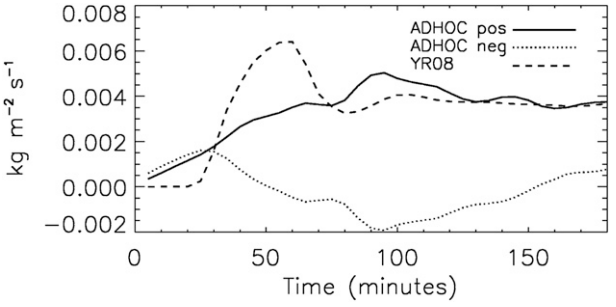

FIG. 10. Comparison of the simulated entrainment rates of ADHOC 3 and SAM for the GCSS smoke cloud case. The positive and negative roots in the entrainment parameterization are shown.

We have shown that we must choose the positive root in Eq. (4.7). For consistency, we must also choose the positive root in the calculation of $\overline{w'w'w'_B}$ in Eq. (3.16). This is plotted in the top panel of Fig. 11. During the initial spinup, ADHOC 3's $\overline{w'w'w'_B}$ lags behind that of SAM. This is correlates to the lower entrainment rate in Fig. 10. Once $\overline{w'w'w'_B}$ in ADHOC catches up to SAM, the entrainment rates are similar as well. In the lower panel of Fig. 11, we show a scatterplot comparing $\overline{w'w'w'_B}$ of ADHOC 3 and SAM at specific times in the simulation. The black diagonal line represents an exact match of the two values. The symbols in red represent values of $\overline{w'w'w'_B}$ during the initial spinup, while those in green are indicative of times later in the simulation. The green symbols are close to the exact-match line, with ADHOC 3 showing slightly larger values for the last hour of the simulation.

c. CTEI case

YR08 studied the cloud-top entrainment instability hypothesis (Lilly 1968; Randall 1980; Deardorff 1980) with SAM under idealized conditions. CTEI is hypothesized to create a positive feedback in PBL turbulence through a process known as buoyancy reversal (Siems et al. 1990). The tests of YR08 are idealized in that turbulence can only grow through buoyancy reversal. Other processes that typically influence stratocumulus clouds are not present (e.g., large-scale subsidence, surface fluxes, shortwave and longwave radiation, and precipitation). One of their results suggest that turbulence produced by CTEI is weaker than that of a typical marine stratocumulus boundary layer.

YR08 tested a variety of idealized cases in SAM with varying cloud-top liquid water mixing ratios and varying virtual potential temperature jumps at the PBL top. For this test case, we chose the case called BR-0.5–73. This case uses a 5-m isotropic grid with a 0.5 g kg^{-1} liquid water mixing ratio at cloud top. It initially has a 4.75-K jump in θ_v and a −6.35 g kg^{-1} jump in total water

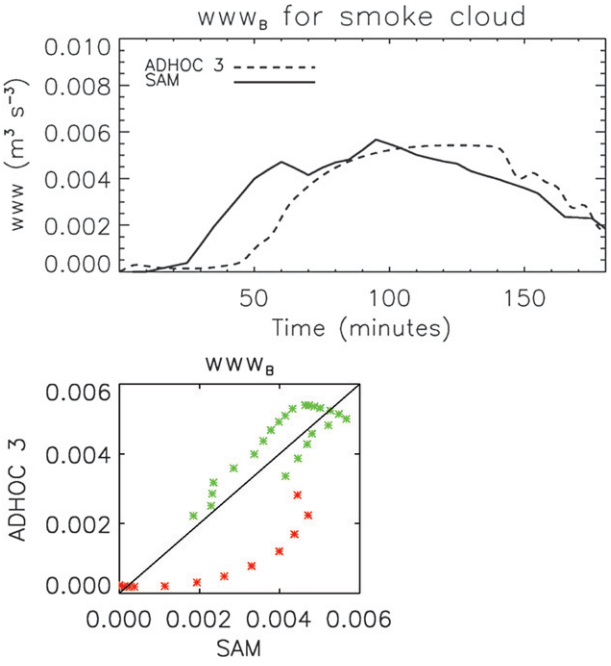

FIG. 11. (top) Comparison of *www* at level B as calculated by Eq. (3.16). We use the positive root because of the results shown in Fig. 10. (bottom) Scatterplot for www at level B comparing ADHOC 3 to LES for various times during the simulation. A perfect correlation is given by the diagonal black line. Red stars indicate the spinup period.

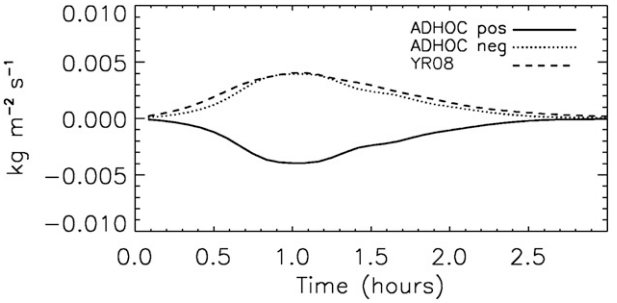

FIG. 12. Comparison of the ADHOC 3 entrainment rate with YR08 for the BR-0.5–73 CTEI case. The positive and negative roots in the entrainment parameterization [Eq. (3.15)] are shown.

mixing ratio. The domain size is 3.2 km horizontally and 1.25 km vertically. The simulation time is 3 h.

For BR-0.5–73, the formula given by Eq. (3.15) also describes the entrainment rate. Here, $C_R = 1$ but $\Delta R = 0$ so the formula for the entrainment rate is identical to that of the clear convective case, with the exception that $\Delta\tau$ in the B term includes the effects of liquid water. Here, $\Delta\tau = \Delta s_v - (\Delta s_v)_{\text{crit}}$ (Randall 1980), where $(\Delta s_v)_{\text{crit}} = [1 - (1 + \delta)\varepsilon/1 + \gamma]L(q^*_{B+} - q_{B+})$, where q^* is the saturation mixing ratio, $\varepsilon = C_pT/L$, $\gamma = (L/C_p)(\partial q^*/\partial T)_p$, and $\delta = 0.608$.

To test the ADHOC 3 entrainment parameterization for this case, we calculate the entrainment rate using Eq. (3.15) and compare it to the entrainment rate diagnosed using the techniques of YR08. This is shown in Fig. 12 with the positive and negative roots of Eq. (3.15). The negative root is clearly correct in the case of marine stratocumulus that exhibit CTEI (negative $\Delta\tau$). The entrainment rate itself is nearly identical to that diagnosed from SAM. Thus, we would expect $\overline{w'w'w'_B}$ to be similar in ADHOC 3 and SAM. In Fig. 13, $\overline{w'w'w'_B}$ in ADHOC 3 does not adjust as quickly as SAM to the decrease in entrainment (between hours 1 and 2). The scatterplot in Fig. 13 shows a good 1-to-1 correspondence between ADHOC 3 and SAM, with the outliers being from the slower adjustment of ADHOC 3 (between hours 1 and 2).

d. *Marine stratocumulus case*

Marine stratocumulus clouds are among the most climatologically important clouds. Small changes in these clouds can significantly alter the amount of solar radiation impinging on the ocean's surface. In climate models, one of the critical issues in parameterizing MSc is accurately representing the entrainment of the overlying warm dry air into these clouds. In this section, we examine the ADHOC 3 entrainment parameterization as applied to the 2003 DYCOMS II RF01 GCSS case (hereafter simply RF01). RF01 is a nocturnal Msc case in which the cloud deck deepened despite macroscopic conditions that would have suggested cloud breakup. [For more detailed information, see http://www.convection.info/blclouds and Stevens et al. (2003).]

The ADHOC 3 simulation of the RF01 case ran for 10 h and had fixed surface fluxes. The time step was 1 s; the vertical resolution was 10 m. The geostrophic wind was specified to be $U_g = 7$ m s^{-1} and $V_g = 5.5$ m s^{-1}. The large-scale divergence of the wind is also specified to be $D = 3.75 \times 10^{-6}$ s^{-1}. Other case details, including the specification of the radiative forcing, are given in the above Web site.

In SAM, the simulation is conducted for the same 10 h. The domain size is 3.36 km horizontally and 1.6 km vertically The grid size is 5 m in the vertical and 35 m in the horizontal. The run is forced with the specifications indicated in the GCSS case setup (see above Web site).

For any stratocumulus case, the ADHOC 3 entrainment parameterization is identical to that of the CTEI case with the exception that ΔR is not equal to zero. Thus, the entrainment rate is given by Eq. (3.15) with $C_R = 1$. For this case, $\Delta\tau$ in the B term includes the effects of liquid water as described in section 4c. To test

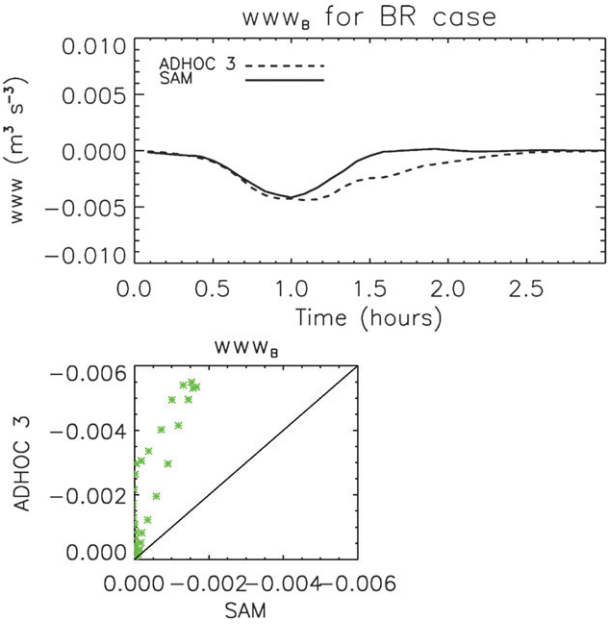

FIG. 13. (top) Comparison of *www* at level B as calculated by Eq. (3.16). We use the negative root because of the results shown in Fig. 12. (bottom) Scatterplot for *www* at level B comparing ADHOC 3 to LES for various times during the simulation. A perfect correlation is given by the diagonal black line.

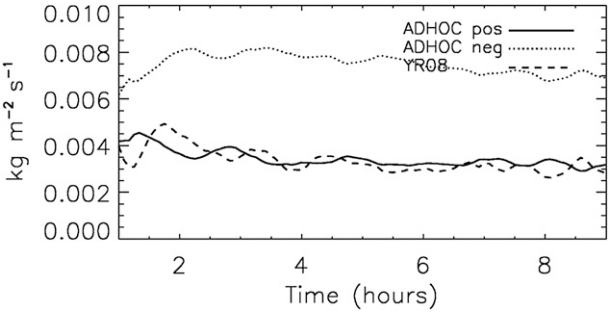

FIG. 14. Comparison of the ADHOC 3 entrainment rate with YR08 for DYCOMS RF01. The positive and negative roots in Eq. (3.15) are shown.

the ADHOC 3 entrainment parameterization for RF01, we calculate the entrainment rate using both the positive and negative roots of Eq. (3.15) and compare it to the entrainment rate diagnosed using the techniques of YR08. This is shown in Fig. 14.

The positive root is correct for stratocumulus, whereas the negative root is correct for the CTEI case. In the RF01 simulations, the radiative jump term dominates the numerator, making the numerator negative. The denominator is dominated by the B term, which is also negative. Thus, both roots give positive entrainment but the positive root agrees with SAM and observational values from DYCOMS (Stevens et al. 2003). In the CTEI case, the denominator was also negative but the ΔR term is equal to zero. Thus, to get positive entrainment, we must choose the negative root for the numerator.

Since we have chosen the positive root in Eq. (3.15), we must also choose the positive root in Eq. (3.16). This means that $\overline{w'w'w'_B}$ is positive for Msc but negative for cloud decks exhibiting CTEI (see previous section). The RF01 values for ADHOC 3 are compared with those diagnosed in SAM in Fig. 15. The agreement is good, with ADHOC 3 tending to slightly underpredict $\overline{w'w'w'_B}$. It should be noted that some observations of DYCOMS (e.g., DYCOMS FLT1) show small negative values of $\overline{w'w'w'_B}$.

5. Sensitivity to vertical resolution

An important aspect of our new ADHOC 3 coordinate is that it can be used with coarser vertical resolution. However, we need to understand changes in the fields that occur when resolution is decreased. In Fig. 16, we use the smoke cloud case and plot the smoke mixing ratio, the vertical heat flux, and the vertical velocity variance as a function of three different vertical resolutions ranging from 10 to 55 PBL layers. The turbulence becomes stronger as the resolution is increased. In fact, increasing the resolution to 55 layers brings the maximum in $\overline{w'w'}$ closer to that obtained in the LES run. (See Fig. 9.) Overall, when we decrease the resolution from 55 to 10 layers, we see a decrease in turbulent intensity in the range of 10%–25%. However, the resulting PBL top height and entrainment rates are well represented in the run with 10 vertical levels (see Figs. 9–10). This is encouraging.

6. Discussion and future work

We have summarized a new method to calculate the entrainment rate in a unified mass-flux/higher-order closure PBL model (ADHOC 3). In previous versions of this stand-alone model (see LRabc), we had to use very high vertical resolution (~20-m grid spacing), mostly in order to resolve sharp jumps at the inversion. To maintain computational stability, we also had to use a very small time step (~0.5 s). Both the high vertical resolution and the correspondingly small time step made ADHOC 3's use in a general circulation model impractical. Here, we have modified ADHOC 3 to use a terrain-following vertical coordinate (σ). With this modification, we can resolve the inversion with significantly coarser vertical resolution and potentially use ADHOC 3 in a GCM. This is our goal.

In the previous z-coordinate versions of ADHOC, entrainment was an implicit quantity. The PBL top rose in response to the turbulence below and we could

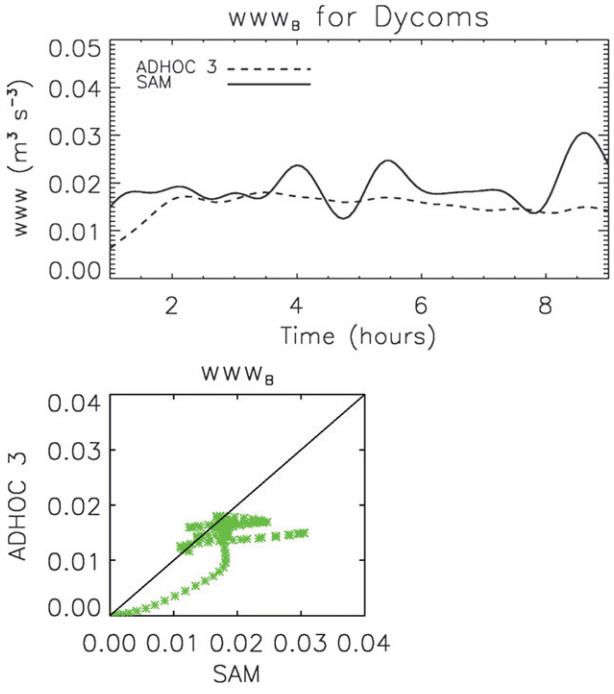

FIG. 15. (top) Comparison of *www* at level B for the RF01 case as calculated by Eq. (3.16). We use the positive root because of the results shown in Fig. 14. (bottom) Scatterplot of *www* at level B in ADHOC 3 and SAM for various times during the simulations.

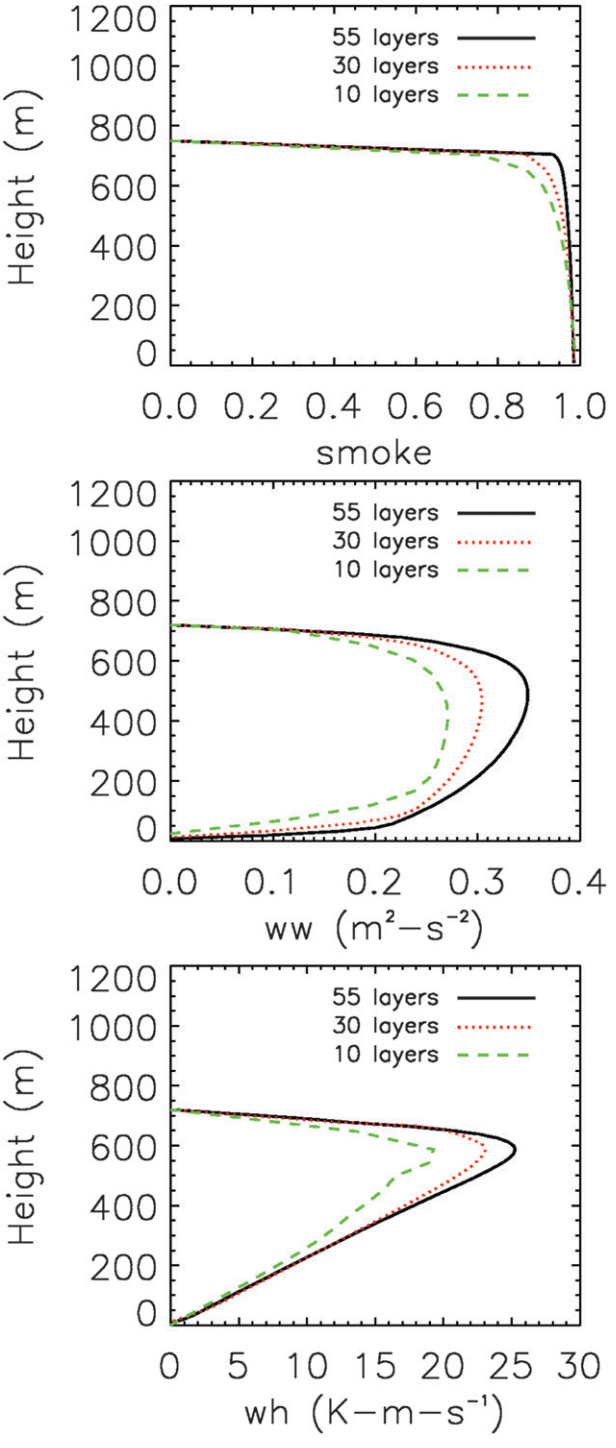

FIG. 16. Comparison of (top) smoke concentration, (middle) vertical velocity variance, and (bottom) vertical heat flux for three different vertical resolutions.

diagnose the entrainment rate from the height change of the PBL top in the model output. With a PBL-top-following coordinate, entrainment enters explicitly and thus must be parameterized.

Most previous entrainment parameterizations proceed from integration of the TKE equation over the PBL. Surface fluxes of heat and radiative cooling are balanced by dissipation and other TKE-consuming processes. This balance is usually parameterized using semiempirical constraints on the relationships between the TKE producing and consuming processes. The resulting formulas depend on the *integrated* TKE available for entrainment. These models include Lilly (1968), Lilly and Schubert (1980), Stage and Businger (1981a,b), Manins and Turner (1978), Deardorff (1976), and BB85. To apply these entrainment formulas, one must know the bulk integrated TKE, but not the turbulent structure within the PBL.

ADHOC 3 predicts the internal structure of the PBL and thus can use this additional information to parameterize the entrainment rate. Here, we developed an entrainment scheme that depends on the second and third moments of the vertical velocity just below the PBL top. ADHOC 3 predicts these moments.

We tested our new scheme with a clear convective, a smoke cloud, a CTEI, and a MSc case. ADHOC 3 was able to accurately represent the evolution of the PBL top height with the new parameterization. For the clear convective and smoke cloud PBLs, it also did a reasonable job depicting the structure of the turbulent boundary layer but did produce weaker turbulence than SAM. An

interesting aspect of these simulations is that ADHOC 3 was able to represent the correct entrainment rate and PBL top evolution with weaker turbulence. This indicates two things. First, the ADHOC 3 entrainment parameterization is very sensitive to $\overline{w'w'}$ and $\overline{w'w'w'}$ (i.e., weaker turbulence leads to bigger responses). Second, the physics embedded in ADHOC 3 will adjust the model correctly to prescribed forcing. In these cases, ADHOC 3 adjusted by "recognizing" the sensitivity of the entrainment rate parameterization to the turbulent structure below it and reducing the strength of the turbulent moments to allow for the correct response.

For our CTEI case, we saw that we must choose the negative root in the entrainment formula. This is because $\Delta\tau$ in the B term is negative because of CTEI. In this case, $\overline{w'w'w'_B}$ in ADHOC 3 did not adjust as quickly to the decrease in the entrainment rate. The entrainment formula for the MSc was similar to the CTEI case with the exception that the radiative jump term was not equal to zero. Here, the cloud did not exhibit CTEI and we chose the positive root. Choosing the roots in this way forces $\overline{w'w'w'_B}$ to be negative in the CTEI case and positive in the MSc (without CTEI) case. This is in agreement with observations.

To use a scheme like this in a large-scale model, we think that the positive root should always be chosen with the exception of cases in which CTEI is confirmed. In the case of the smoke cloud (where $\Delta R > 0$), it is possible to achieve positive entrainment with the negative root. However, we have tested a range of values of values for the numerator's terms and found that the $\overline{w'w'_B}$ term is always larger than the ΔR term [Eq. (3.15)]. As ΔR gets larger, $\overline{w'w'_B}$ also gets larger and this remains true. In all cases that exhibit CTEI, $\Delta\tau < 0$ and this dominant term makes the denominator negative. In these cases, we find the negative root must be chosen so that the entrainment remains positive. The choice of sign, however, still remains an issue. We have not concluded with 100% certainty that there are not cases in which both signs will provide valid solutions. This will be analyzed in the future as we conduct new case studies to test the ideas.

Our new approach can and will be extended to stratocumulus-topped PBLs. However, the next *major* step in the evolution of ADHOC is to move away from the top-hat model and introduce a more realistic and flexible assumed joint distribution of the variables. The top-hat distribution has known deficiencies in the representation of higher-order moments (Wang and Stevens 2000). Thus, this is the most important remaining problem to be addressed.

Acknowledgments. This work has been supported by the National Science Foundation and Technology Center for Multi-Scale Modeling of Atmospheric Processes, managed by Colorado State University under Cooperative Agreement ATM-0425247. Acknowledgment is made to the National Center for Atmospheric Research, which is sponsored by the National Science Foundation, for the computing time used in this research.

APPENDIX

Finite Differencing in ADHOC 3

The mean state and the third moments are defined at different locations than the second moments and the vertical advection $\dot{\sigma}$. (See Fig. A1.) This facilitates easier finite differencing of the turbulent transport and vertical advection of the mean state. The vertically discrete continuity equation in such a system is

$$\frac{\partial \pi}{\partial t} + \nabla \cdot (\pi \mathbf{v}_k) + \frac{\pi\dot{\sigma}_{k+1/2} - \pi\dot{\sigma}_{k-1/2}}{\delta\sigma_k} = 0, \quad \text{(A.1)}$$

where k is the layer index. (See Fig. A1.) If we sum Eq. (2.9) over all PBL layers, the last term gives us contributions from only the surface and the PBL top layers. Since $(\pi\dot{\sigma})_S = 0$, we can write

$$\sum_k (\delta\sigma)_k \frac{\partial \pi}{\partial t} + \sum_k \pi(\nabla \cdot \mathbf{v})_k \delta\sigma_k = g(E - M_B), \quad \text{(A.2)}$$

where g is the acceleration of gravity, E is the entrainment rate, and M_B is the cumulus mass flux (Arakawa

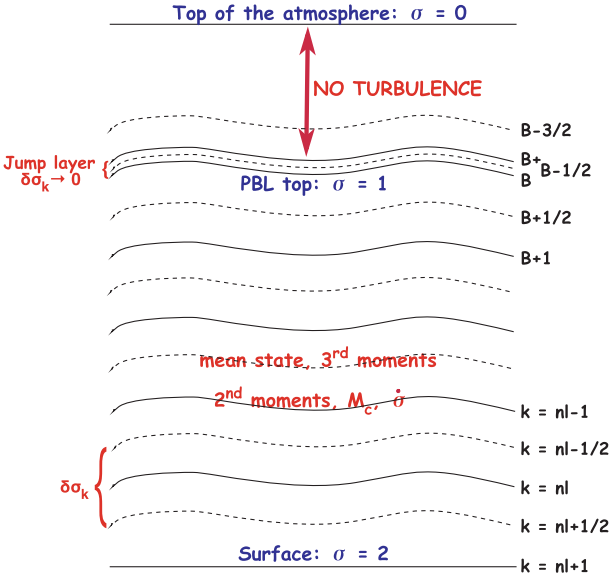

FIG. A1. The vertical grid, showing the indexing scheme. The PBL top is treated as a "virtual layer," with zero thickness. The layers above the PBL top are not shown.

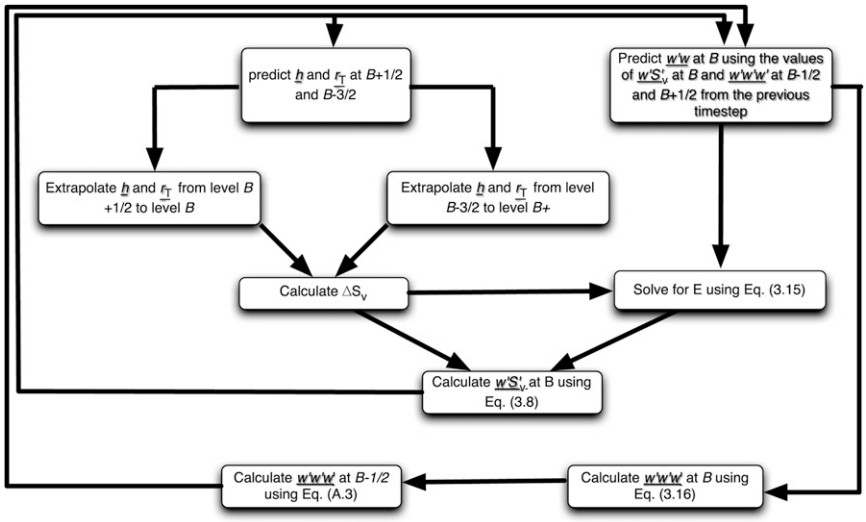

FIG. A2. Flowchart outlining the upper boundary conditions in ADHOC 3.

and Schubert 1974). Here we have introduced the approximation $\nabla \cdot \sum_k (\pi \mathbf{v})_k \delta\sigma_k \simeq \sum_k \pi (\nabla \cdot \mathbf{v})_k \delta\sigma_k$, which is used only in our single-column tests.

In ADHOC 3, we predict the PBL thickness, π, using Eq. (2.10). Then we use $\partial\pi/\partial t$ in Eq. (2.9) to get $\pi\dot{\sigma}$ at each level. Finally, we use these $\pi\dot{\sigma}$ values to do vertical advection in all our prognostic equations. The $\delta\sigma_k$ values are preset but we need to update the pressure and height thicknesses of the layers after each time step.

Finally, the manner in which the finite difference model handles boundary conditions at the infinitesimal top layer is shown in a flowchart in Fig. A2. ADHOC 3 predicts $\overline{w'w'_B}$. In the prognostic equation for this, we need to know the divergence, $\overline{w'w'w'_{B-1/2}} - \overline{w'w'w'_{B+1/2}}$. The second term is predicted, while the latter term is approximated using

$$\overline{w'w'w'_{B-1/2}} = 0.5 \times \overline{w'w'w'_B}. \qquad \text{(A.3)}$$

ADHOC 3 also predicts the moist static energy and total water mixing ratio at levels $B + \frac{1}{2}$ and $B - \frac{3}{2}$. We linearly extrapolate these values to levels to levels B and $B+$. We then use these values to calculate the virtual static energy jump across the PBL top layer $(\Delta s_v)_B$. This and the predicted value of $\overline{w'w'_B}$ are used to calculate the entrainment rate in Eq. (3.15). This entrainment rate is then used in the calculation of $\overline{w'S'_{vB}}$, which is then used to predict the new value of $\overline{w'w'_B}$.

REFERENCES

André, J. C., G. DeMoor, P. Lacarrère, G. Therry, and R. Du Vachat, 1978: Modeling the 24-hour evolution of the mean and turbulent structures of the planetary boundary layer. *J. Atmos. Sci.,* **35,** 1861–1883.

Arakawa, A., and W. H. Schubert, 1974: Interaction of a cumulus cloud ensemble with the large-scale environment, Part I. *J. Atmos. Sci.,* **31,** 674–701.

Ball, F. K., 1960: Control of inversion height by surface heating. *Quart. J. Roy. Meteor. Soc.,* **86,** 483–494.

Breidenthal, R. E., and M. B. Baker, 1985: Convection and entrainment across stratified interfaces. *J. Geophys. Res.,* **90,** 13 055–13 062.

Bretherton, C. S., and Coauthors, 1999: An intercomparison of radiatively driven entrainment and turbulence in a smoke cloud, as simulated by different numerical models. *Quart. J. Roy. Meteor. Soc.,* **125,** 391–423.

Businger, J. A., and S. P. Oncley, 1990: Flux measurements with conditional sampling. *J. Atmos. Oceanic Technol.,* **7,** 349–352.

Clark, R. H., A. J. Dyer, R. R. Brook, D. G. Reid, and A. J. Troup, 1971: The Wangara experiment: Boundary layer data. Tech. Paper 19, Division of Meteorology and Physics, CSIRO, Australia, 38 pp.

Deardorff, J. W., 1972: Parameterization of the planetary boundary layer for use in general circulation models. *Mon. Wea. Rev.,* **100,** 93–106.

——, 1976: On the entrainment rate of a stratocumulus-topped mixed layer. *Quart. J. Roy. Meteor. Soc.,* **102,** 563–582.

——, 1980: Cloud top entrainment instability. *J. Atmos. Sci.,* **37,** 131–147.

de Laat, A. T. J., and P. G. Duynkerke, 1998: Analysis of ASTEX stratocumulus observational data using a mass-flux approach. *Bound.-Layer Meteor.,* **86,** 63–87.

de Roode, S. R., P. G. Duynkerke, and A. P. Siebesma, 2000: Analogies between mass-flux and Reynolds-averaged equations. *J. Atmos. Sci.,* **57,** 1585–1598.

Kahn, P. H., and J. A. Businger, 1979: The effects of radiative flux divergence on entrainment of a saturated convective boundary layer. *Quart. J. Roy. Meteor. Soc.,* **105,** 303–306.

Kasahara, A., 1974: Various vertical coordinate systems used for numerical weather prediction. *Mon. Wea. Rev.,* **102,** 509–522.

Khairoutdinov, M., and D. A. Randall, 2003: Cloud-resolving modeling of the ARM summer 1997 IOP: Model formulation, results, uncertainties, and sensitivities. *J. Atmos. Sci.,* **60,** 607–625.

Konor, C. S., and A. Arakawa, 1997: Design of an atmospheric model based on a generalized vertical coordinate. *Mon. Wea. Rev.,* **125,** 1645–1673.

——, G. C. Boezio, C. R. Mechoso, and A. Arakawa, 2009: Parameterization of PBL processes in an atmospheric general circulation model: Description and preliminary assessment. *Mon. Wea. Rev.,* **137,** 1061–1082.

Lappen, C.-L., and D. A. Randall, 2001a: Toward a unified parameterization of the boundary layer and moist convection. Part I: A new type of mass-flux model. *J. Atmos. Sci.,* **58,** 2021–2036.

——, and ——, 2001b: Toward a unified parameterization of the boundary layer and moist convection. Part II: Lateral mass exchanges and subplume-scale fluxes. *J. Atmos. Sci.,* **58,** 2037–2051.

——, and ——, 2001c: Toward a unified parameterization of the boundary layer and moist convection. Part III: Simulations of clear and cloudy convection. *J. Atmos. Sci.,* **58,** 2052–2072.

——, and ——, 2005: Using idealized coherent structures to parameterize momentum fluxes in a PBL mass-flux model. *J. Atmos. Sci.,* **62,** 2829–2846.

——, and ——, 2006: Parameterization of pressure perturbations in a PBL mass-flux model. *J. Atmos. Sci.,* **63,** 1726–1751.

Lilly, D. K., 1968: Models of cloud-topped mixed layers under a strong inversion. *Quart. J. Roy. Meteor. Soc.,* **94,** 292–309.

——, and W. H. Schubert, 1980: The effects of radiative cooling in a cloud-topped mixed layer. *J. Atmos. Sci.,* **37,** 482–487.

Manins, P. C., and J. S. Turner, 1978: The relation between the flux ratio and energy ratio in convectively mixed layers. *Quart. J. Roy. Meteor. Soc.,* **104,** 39–44.

Medeiros, B., A. Hall, and B. Stevens, 2005: What controls the mean depth of the PBL? *J. Climate,* **18,** 3157–3172.

Mellor, G. L., 1977: The Gaussian cloud model relations. *J. Atmos. Sci.,* **34,** 356–358.

——, and T. Yamada, 1974: A hierarchy of turbulence closure models for planetary boundary layers. *J. Atmos. Sci.,* **31,** 1791–1806.

Millionshchikov, M. D., 1941: On the theory of homogeneous isotropic turbulence. *Dokl. Akad. Nauk SSSR,* **32,** 611–614.

Miyakoda, K., and J. Sirutis, 1977: Comparative integrations of global models with various parameterized processes of subgrid-scale vertical transports: Description of the parameterizations. *Beitr. Phys. Atmos.,* **50,** 445–487.

Moeng, C.-H., 1984: A large-eddy simulation model for the study of planetary boundary-layer turbulence. *J. Atmos. Sci.,* **41,** 2052–2062.

——, S. Shen, and D. A. Randall, 1992: Physical processes within the nocturnal stratus-topped boundary layer. *J. Atmos. Sci.,* **49,** 2384–2401.

——, P. P. Sullivan, and B. Stevens, 1999: Including radiative effects in an entrainment rate formula for buoyancy-driven PBLs. *J. Atmos. Sci.,* **56,** 1031–1049.

Nieuwstadt, F. T., and J. A. Businger, 1984: Radiative cooling near the top of a cloudy mixed layer. *Quart. J. Roy. Meteor. Soc.,* **110,** 1073–1078.

Petersen, A. C., C. Beets, H. van Dop, P. G. Duynkerke, and A. P. Siebesma, 1999: Mass-flux characteristics of reactive scalars in the convective boundary layer. *J. Atmos. Sci.,* **56,** 37–56.

Randall, D. A., 1976: The interaction of the planetary boundary layer with large-scale circulations. Ph.D. thesis, Department of Atmospheric Sciences, University of California, Los Angeles, 214 pp.

——, 1980: Conditional instability of the first kind upside-down. *J. Atmos. Sci.,* **37,** 125–130.

——, 1987: Turbulent fluxes of liquid water and buoyancy in partly cloudy layers. *J. Atmos. Sci.,* **44,** 850–858.

——, J. A. Abeles, and T. G. Corsetti, 1985: Seasonal simulations of the planetary boundary layer and boundary-layer stratocumulus clouds with a general circulation model. *J. Atmos. Sci.,* **42,** 641–676.

——, Q. Shao, and C.-H. Moeng, 1992: A second-order bulk boundary-layer model. *J. Atmos. Sci.,* **49,** 1903–1923.

Schubert, W. H., J. S. Wakefield, E. J. Steiner, and S. K. Cox, 1979: Marine stratocumulus convection. Part I: Governing equations and horizontally homogeneous solutions. *J. Atmos. Sci.,* **36,** 1286–1307.

Siems, S. T., C. S. Bretherton, M. B. Baker, S. Shy, and R. E. Breidenthal, 1990: Buoyancy reversal and cloud-top entrainment instability. *Quart. J. Roy. Meteor. Soc.,* **116,** 705–739.

Sommeria, G., and J. W. Deardorff, 1977: Subgrid-scale condensation in models of non-precipitating clouds. *J. Atmos. Sci.,* **34,** 344–355.

Stage, S. A., and J. A. Businger, 1981a: A model for entrainment into a cloud-topped marine boundary layer. Part I: Model description and application to a cold-air outbreak episode. *J. Atmos. Sci.,* **38,** 2213–2229.

——, and ——, 1981b: A model for entrainment into a cloud-topped marine boundary layer. Part II: Discussion of model behavior and comparison with other models. *J. Atmos. Sci.,* **38,** 2230–2242.

Stevens, B., 2002: Entrainment in stratocumulus-topped mixed layers. *Quart. J. Roy. Meteor. Soc.,* **128,** 2663–2690.

——, and Coauthors, 2003: On entrainment rates in nocturnal marine stratocumulus. *Quart. J. Roy. Meteor. Soc.,* **129,** 3469–3493.

Suarez, M. J., A. Arakawa, and D. A. Randall, 1983: The parameterization of the planetary boundary layer in the UCLA general circulation model: Formulation and results. *Mon. Wea. Rev.,* **111,** 2224–2243.

Wang, S., and B. Stevens, 2000: Top-hat representation of turbulence statistics in cloud-topped boundary layers: A large-eddy simulation study. *J. Atmos. Sci.,* **57,** 423–441.

Willis, G. E., and J. W. Deardorff, 1974: A laboratory model of the unstable planetary boundary layer. *J. Atmos. Sci.,* **31,** 1297–1307.

Wyngaard, J. C., and C.-H. Moeng, 1992: Parameterizing turbulent diffusion through the joint probability density. *Bound.-Layer Meteor.,* **60,** 1–13.

Yamaguchi, T., and D. A. Randall, 2008: Large-eddy simulation of evaporatively driven entrainment in cloud-topped mixed layers. *J. Atmos. Sci.,* **65,** 1481–1504.

Young, G. S., 1988: Turbulence structure of the convective boundary layer. Part II: Phoenix 78 aircraft observations of thermals and their environment. *J. Atmos. Sci.,* **45,** 727–735.